

Development of a Passive Compliant Mechanism for Measurement of Micro/Nano-Scale Planar Three DOF Motions

Leon Clark¹, Bijan Shirinzadeh¹, Yanling Tian², and Bin Yao³

Abstract

This paper presents the design, optimization, and computational and experimental performance evaluations of a passively actuated, monolithic, compliant mechanism. The mechanism is designed to be mounted on or built into any precision positioning stage which produces three degree of freedom (DOF) planar motions. It transforms such movements into linear motions which can then be measured using laser interferometry based sensing and measurement techniques commonly used for translational axes. This methodology reduces the introduction of geometric errors into sensor measurements, and bypasses the need for increased complexity sensing systems. A computational technique is employed to optimize the mechanism's performance, in particular to ensure the kinematic relationships match a set of desired relationships. Computational analysis is then employed to predict the performance of the mechanism throughout the workspace of a coupled positioning stage, and the errors are shown to vary linearly with the input position. This allows the errors to be corrected through calibration. A prototype is manufactured and experimentally tested, confirming the ability of the proposed mechanism to permit measurements of three DOF motions.

Keywords: micro/nano positioning, coupled 3DOF motion, laser interferometer based sensing

1 Introduction

Manipulation and positioning at the micro- and nano-scales has been identified as one of the key foundations of modern nanotechnology. It plays a major role in many recent and proposed technologies including scanning probe microscopy, micro-grasping, optical alignment, microscale manufacturing and assembly, and lithography [1–6].

Flexure-based mechanisms actuated by piezoelectric actuators (PEAs) are commonly employed to facilitate the production of such high precision motions. The design of such mechanisms using compliant

This work was supported by ARC LIEF (Grants LE0347024, and LE0775692), and ARC Discovery Projects (Grants DP110104970, and DP140104019). This work was performed in part at the Melbourne Centre for Nanofabrication (MCN) in the Victorian Node of the Australian National Fabrication Facility (ANFF).

¹ L. Clark and B. Shirinzadeh are with the Robotics and Mechatronics Research Laboratory, Department of Mechanical and Aerospace Engineering, Monash University, Clayton, VIC 3800, Australia (email: leon.clark@monash.edu, bijan.shirinzadeh@monash.edu).

² Y. Tian is with the Key Laboratory of Mechanism Theory and Equipment Design of Ministry of Education, Tianjin University, Tianjin 30072, China (email: meytian@tju.edu.cn).

³ B. Yao is with the School of Mechanical Engineering, Purdue University, West Lafayette, Indiana (email: byao@purdue.edu).

This is a post-print version of: L. Clark, B. Shirinzadeh, Y. Tian, and B. Yao. Development of a Passive Compliant Mechanism for Measurement of Micro/Nano-Scale Planar Three DOF Motions. *IEEE/ASME Transactions on Mechatronics*, 2015, DOI: 10.1109/TMECH.2015.2503728.

elements including flexure hinges and flexural cantilevers has gained considerable attention. They permit motion free from numerous effects which hinder the use of pinned joints including friction, backlash and wear. Furthermore, they allow the monolithic construction of mechanisms, which reduces the possibility of assembly errors. Consequently, mechanisms which produce translational motion with one, two and three degrees of freedom (DOFs) have been proposed [7–10]. However, flexure hinges are not ideal revolute joints, and the pivoting of a hinge will be accompanied by a translation of the rotation center, as well as possible out-of-plane motions. For this reason, many hinge geometries have been proposed, some with an emphasis on rotational precision, at the cost of stress concentration, whilst others are more compliant [11, 12].

As these flexure-based mechanisms are typically actuated with PEAs, hysteresis and drift are introduced into the input-output response. For this reason, considerable attention has been directed towards the design of control methodologies. These include feedback strategies, such as sliding mode control, adaptive control, and model predictive control [13–17]; capacitance and charge based control of PEAs [18]; in addition to schemes employing inversions of the hysteresis models [19, 20].

To this end, non-contact measurement methods such as capacitive plate sensing and laser interferometry based sensing have been implemented for feedback control. Of these two, laser interferometry based techniques are promising, as they offer high resolution measurement, traceable to the standards of measurement, over a large range and at a high rate. Recent studies have demonstrated their applicability for feedback control purposes at the micro/nano scale [21].

The accuracy of both capacitive and laser interferometry based sensing and measurement techniques are affected by the introduction of misalignment. In the case of interferometry based systems, misalignment introduces geometric errors, the most common being cosine and Abbe errors. Being approximately linearly proportional to the misalignment angle, Abbe errors are typically the dominant type of geometric error. Large misalignments can be sufficient to deflect a measurement beam from the photo-detector, thus ceasing functionality completely. Hence, for linear stages, it is necessary to ensure that cross-coupled angular motion is minimized.

Recent research on the design of compliant mechanisms has resulted in the production of stages with higher degrees of freedom. In particular, this has led to stages which perform angular motion in addition to linear motion [22, 23]. Commonly, these stages have three planar DOFs, due to limitations in fabrication processes [24–27].

High precision measurement of the rotational axis can be performed using autocollimators, interferometers and position sensitive diode based sensors [28–31]. However, there is difficulty in measuring the coupled linear motions, as the production of angular motion and subsequent misalignments introduces geometric errors within measurement. Kim et al. [32] proposed a compact hybrid interferometry-autocollimator system capable of measurement of a linear and angular axis, however its reported angular range of 0.29 mrad is insufficient for most existing linear-angular stages. Zhang and Menq [33] developed a large range interferometer using retro-reflectors, which has a practically unlimited angular range. However, offsets within the sensor imposed large Abbe errors on linear measurement. Hence, this sensor would require calibration specific to each application of the sensor. For this reason, earlier studies often considered angular motion as an error, upon which the additional rotational DOFs could be actuated to eliminate [34–36].

In the authors' previous work, a mechanical means of minimizing misalignment has been introduced [37]. This utilized a beam steering assembly beneath the flexure mechanism to ensure the continuous alignment of the measurement beams. Measurement throughout the full mechanism workspace could then proceed, with minimal geometric errors.

This paper presents the mechanical design and evaluation of a mechanism which seeks to prevent the misalignment of the measurement beams. The proposed design provides a novel mechanical approach as a counterpart to more complex optical systems. In particular, the mechanism allows measurement

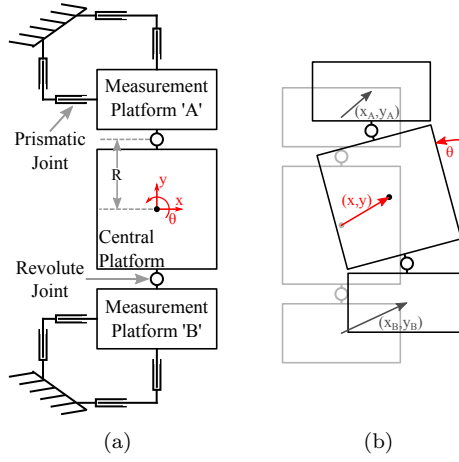


Figure 1: Rigid body schematic of the proposed mechanism: (a) Undisturbed mechanism, (b) Mechanism response to coupled X , Y and θ motions.

of both linear and angular axes using only linear interferometer-based sensing techniques which are commonly employed in micro/nano positioning. As a result, the proposed methodology inherits the speed and resolution of interferometry based measurement techniques, and is shown to have high accuracy post-calibration, without burdening the positioner's dynamic performance. To this end, this passive mechanism achieves the benefits found through the previous work, without requiring the addition of extra actuated axes and a rotation sensor.

2 Mechanism Design

A flexure-based parallel mechanism has been designed to transform planar three DOF motion into translations accessible to linear axes of laser interferometry based sensing and measurement techniques. A rigid-body conceptual schematic of this mechanism is shown in Fig. 1a. The central platform of this mechanism is coupled to the end effector of a positioning stage. When the stage produces coupled planar motions, the mechanism will displace as shown in Fig. 1b. The two measurement platforms, one above and one below the central platform are constrained to move linearly without any rotation by the chain of prismatic joints connecting each platform to the base. The change in each platform's position is therefore determined by the position of the revolute joint which links it to the central platform. The change in each platform's position is therefore given by:

$$\begin{aligned} \begin{bmatrix} x_A \\ y_A \end{bmatrix} &= \begin{bmatrix} \cos \theta & -\sin \theta \\ \sin \theta & \cos \theta \end{bmatrix} \begin{bmatrix} 0 \\ R \end{bmatrix} + \begin{bmatrix} x \\ y \end{bmatrix} - \begin{bmatrix} 0 \\ R \end{bmatrix} \\ &= \begin{bmatrix} x - R \sin \theta \\ y + R \cos \theta - R \end{bmatrix} \end{aligned} \quad (1)$$

$$\begin{bmatrix} x_B \\ y_B \end{bmatrix} = \begin{bmatrix} x + R \sin \theta \\ y - R \cos \theta + R \end{bmatrix} \quad (2)$$

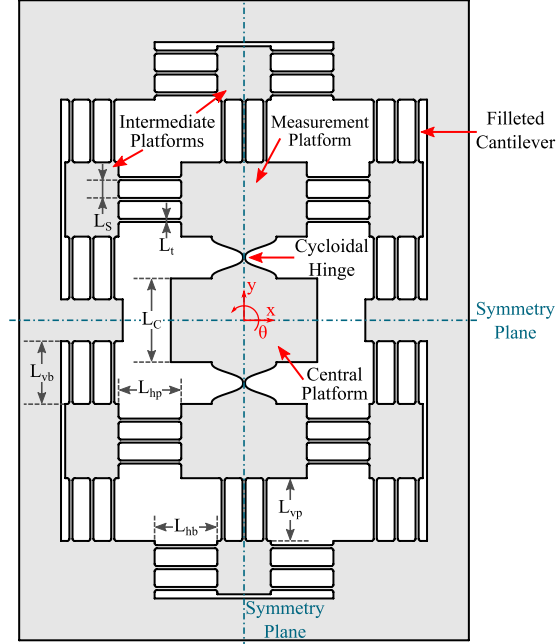


Figure 2: Flexure design of mechanism showing design parameters for optimization.

These two equations can be readily solved to produce the position of the central platform:

$$x = \frac{1}{2}(x_A + x_B) \quad (3)$$

$$y = \frac{1}{2}(y_A + y_B) \quad (4)$$

$$\theta = \arctan\left(\frac{x_B - x_A}{y_A - y_B + 2R}\right) \approx \frac{x_B - x_A}{2R} \quad (5)$$

These equations, which will be referred to as the *desired kinematics*, show that in ideal conditions, the position of the central platform can be determined simply from the position of the measurement platforms. In practice, to prevent the overuse of interferometer axes, y could instead be estimated using the computation of (5):

$$y \approx y_A + R \left[1 - \cos\left(\frac{x_B - x_A}{2R}\right) \right] \quad (6)$$

The flexure-based design of the mechanism is shown in Fig. 2. Within the mechanism, the parallelogram flexure configuration has been exploited to construct prismatic elements. These consist of parallel filletted cantilevers. The mechanism is designed to have symmetry about each of the coordinate planes, which adds redundancy to the mechanism. In effect, this minimizes the rotation of each of the measurement platforms. The cantilevers about each intermediate platform similarly have equal length. Furthermore, each parallelogram flexure consists of three parallel cantilevers to reduce the rotation of the intermediate platforms.

The two flexure hinges which link the measurement platforms to the central platform are of a cycloidal geometry, as illustrated in Fig. 3. It has been shown that these hinges have higher relative rotational precision than circular hinges [11]. The profile of one side of the hinge is expressed by the parametric

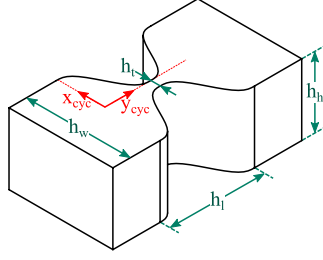


Figure 3: Geometry of a cycloidal hinge.

curve (7), with $t \in [0, 1]$:

$$x_{cyc}(t) = (h_w - h_t) \left[\left| t - \frac{1}{2} \right| - \frac{1}{4\pi} \sin \left(4\pi \left| t - \frac{1}{2} \right| \right) \right] + \frac{h_t}{2} \quad (7a)$$

$$y_{cyc}(t) = h_l t \quad (7b)$$

3 Design Optimization

The transition from the rigid body components to their flexure-based equivalents comes at the cost of introducing compliance into the mechanism. Hence, the motion of the central platform and the consequent displacement of the measurement platforms will be resisted by the hinges and cantilevers. As a result, the desired behavior will not be exhibited perfectly. The choice of the design parameters, which has direct influence over the stiffnesses of each flexure component, becomes critical in determining the performance of the mechanism.

Consequently, optimization of the design, through the selection of the design parameters has been performed. Due to the difficulty in producing an analytical model of the mechanism, a computational approach has been adopted. All parameters defined in Figs. 2 and 3 were considered to be variables, except for the mechanism height (h_h) which was chosen to be 10 mm, and the cantilever fillet radius of 0.5 mm.

Two objectives were considered for the design optimization:

1. To minimize the difference between the central platform position and those calculated by (3), (4), (5); and,
2. To minimize the rotation of the two measurement platforms.

The cost function for these objectives was defined as the L^1 norm of the error ratios of the outputs of (3)-(5), together with the misalignment of the measurement platforms:

$$C = \left| \frac{x - x_c}{x_c} \right| + \left| \frac{y - y_c}{y_c} \right| + \left| \frac{\theta - \theta_c}{\theta_c} \right| + \eta(|\alpha_A| + |\alpha_B|) \quad (8)$$

where α represents the misalignment of a measurement platform, (x_c, y_c, θ_c) is the computationally determined central platform pose, and η is a non-negative weighting factor.

The optimization was further constrained by the maximum allowable stress, limitations on the thickness of the hinges and cantilevers, in addition to the size constraints of the entire mechanism. To this end, the initial parameter space was chosen to contain a wide range of potential designs satisfying these constraints. Table 1 shows the initial range of each parameter.

Table 1: Initial design space

Design parameter	Variable	Minimum	Maximum
Hinge thickness	h_t	0.3 mm	1.0 mm
Hinge (half) width	$0.5h_w - h_t$	3.5 mm	10 mm
Hinge length	h_l	3.5 mm	10 mm
Platform length	L_C	16 mm	40 mm
Cantilever thickness	L_t	0.3 mm	1.0 mm
Cantilever spacing	L_S	5.0 mm	14 mm
Cantilever lengths	$L_{vb}, L_{hb}, L_{vp}, L_{hp}$	5.0 mm	25 mm

The operating range was chosen to match that of a three DOF planar positioning stage based upon the three revolute-revolute-revolute (3-RRR) kinematic chain, which was utilized for the experimental validation, to be described in Section 6. The workspace is approximately 160 μm in the X -direction, 183 μm in the Y -direction, and 5.5 mrad in θ .

3.1 Computational Model

Finite element analysis has been utilized to perform computational analysis of each candidate design. The meshed model of the mechanism is shown in Fig. 4. A planar model has been utilized for this analysis to maximize the number of in-plane nodes. As the geometric model varied with the design parameters, the model was re-meshed for each point in the design space. The meshed model focused on increasing the number of elements around the cantilevers and flexure hinges. At least four elements spanned each hinge and cantilever. The exact number of nodes varied between each design, but generally the mesh contained in excess of 60,000 nodes and 55,000 elements. The properties of aluminum alloy 7075-T6, which is commonly used to fabricate compliant mechanisms, was assumed for the computational optimization.

Measurements were performed by determining the average displacements of collections of nodes around small holes centered on each platform. Instead of simply applying the displacement input to these nodes on the central platform, inputs have been applied at two opposite corners of the platform. This ensured that the stresses around the measurement nodes were small, hence these nodes' locations are a better representation of the central platform's displacement.

The input which was utilized for the computational analysis of each set of design parameters was chosen to be $(x, y, \theta) = (-5 \mu\text{m}, 5 \mu\text{m}, 0.5 \text{ mrad})$. This was considered to be a representative point within the desired workspace.

4 Optimization Procedure

The response surface methodology was initially utilized for this study. However, the widths of supports within the mechanism were dependent on the differences between the design parameters. For example, with regards to Fig. 2, the widths of the supports in the corners of the mechanism depended on the difference between L_{hp} and L_{hb} . Beneath a lower bound of this difference, the design became infeasible. It was found that often the fitted response surface would identify a minimum in the infeasible region of the design space. Therefore, the process using response surfaces had to be abandoned.

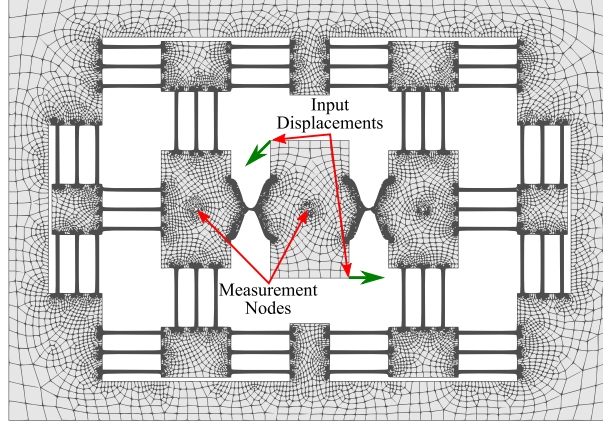


Figure 4: Meshed model of mechanism for optimization through computational analysis. Input displacement vectors applied to the central platform are indicated in green.

Instead, the design space was uniformly sampled by a large number of design points. In this process, design points both within and outside the feasible region were attempted to be solved computationally.

As only a finite number of points were sampled from the continuous design space, the design point which minimizes C would almost certainly never be sampled. Instead, each design point would be a certain distance from this optimum point. As the design space is uniformly sampled, the shortest radius of a sampled point in the N dimensional design space from the optimum design can be approximated. Translating and scaling each design variable into the interval $[0, 1]$, the design space can be considered as an N dimensional hypercube. Hence, when the space is uniformly sampled by n_s points, each point can be considered to occupy a hypercube of side length:

$$\beta_{\text{SFF}} = \frac{1}{\sqrt[n]{n_s}} \quad (9)$$

This *space filling factor* provides a measure of how close the best design point from the n_s samples is to the optimum design. Hence, 2^{10} samples are required to reduce the range of each design variable by a half when there are ten variables.

As a consequence of the slow rate of decrease of β_{SFF} with respect to n_s , the sampling of the design space was halted once β_{SFF} was lower than approximately 0.5. The range of each design variable was reduced by this factor which would reduce unnecessary sampling in non-optimal regions. Furthermore, if a trend was seen between C and a design variable, that design variable was eliminated from sampling. In particular, $C_{\eta=0}$ was seen to decrease with decreasing h_t and L_C , and hence these variables were fixed at their minimum allowable values in iterations 2 and 3 respectively. This further reduced the number of samples needed. Some of the trends observed during the optimization procedure were (ordered from strongest trend to weakest):

- The measurement error correlates with the platform misalignment;
- The overall error decreased as the cantilever thickness was reduced;
- The overall error decreased as the hinge thickness was reduced;
- The overall error decreased as the ratio of the hinge width to length was increased;
- Increasing L_{vp} reduced the error for X and θ , whilst also reducing platform misalignment;
- The overall error reduced as the central platform height L_C was increased;

Table 2: Summary of design space sampling iterations

Iteration	Variables	Points	Feasible	$C_{\eta=0,\min}$	$\beta_{\text{SFF,rel}}$
1	10	1028	523	2.23%	0.500
2	9	581	451	1.27%	0.246
3	8	740	535	1.07%	0.108

Table 3: Stability of simulation for design candidates

	Samples	$E(C_{\eta=0})$	$SE(C_{\eta=0})$	$\sigma(C_{\eta=0})$
Candidate 1	15	1.27%	0.13%	0.49%
Candidate 3	17	1.39%	0.13%	0.53%
Final design	5	1.72%	0.05%	0.11%

- Increasing L_{vb} reduced the error for X and θ ;
- The error for X and θ and the platform misalignment decreased as the cantilever spacing L_S was increased;
- Increasing L_{hb} reduced the error for Y ; and,
- Increasing L_{hp} reduced the Y error, however this slightly increased platform misalignment and error in X and θ .

Table 2 shows the progression of the design during the sampling phase of the optimization. The last column, $\beta_{\text{SFF,rel}}$, provides the space filling factor relative to the initial design space (where $\beta_{\text{SFF}} = 1$).

As can be seen from Table 2, the proportion of feasible points increased between each iteration. For the last iteration, it was found that feasible design candidates could be determined through a fitted response surface. This was performed using a multi-objective genetic algorithm to find a minimum point on a response surface determined using the kriging interpolation method.

Three design candidates were selected from the response surface, of which the second was found to be infeasible. At this stage, the predictions of the response surface were verified through simulation with the existing model. In particular, for both of the remaining candidates the model was repeatedly re-meshed to examine the sensitivity to the numerical model. Table 3 shows the sample mean cost, together with the standard error (the estimated deviation of this mean from the population mean), as well as the sample standard deviation.

It can be seen from Table 3 that the predictions of the computational analysis are greatly affected by the meshed model of the optimized designs. This was found to be caused by the supports within these designs being too thin. Consequently, the central platform's height was increased, widening these components, producing the final design shown in Fig. 5. Further sampling showed the simulation outputs were much more stable with this design. However, it can be seen from Table 3 that the final design suffers from a degradation in performance.

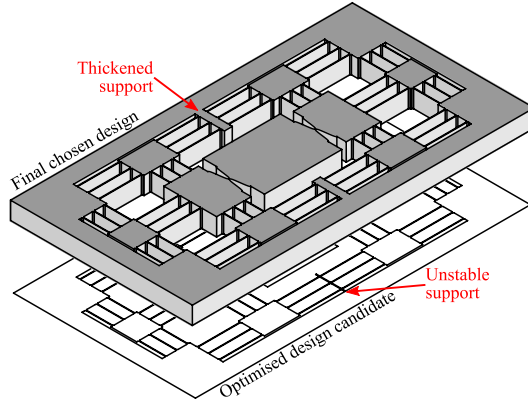


Figure 5: Modification of the optimized design candidate for the final chosen design. Note that the supports on the longer sides of the mechanism have been thickened.

5 Computational Validation Study

5.1 Error Variation

In the optimization study, the mechanism input displacement was fixed as design parameters were varied. Hence, whilst the overall goal of the design was to minimize errors over all inputs, the optimization only focused on this minimization at the single fixed point.

It is therefore important to examine the variation of the error throughout the entire space of inputs. Simulations were performed on uniformly spaced points throughout the designed workspace of the 3-RRR positioner. This was produced by generating the points within the output range of the actuators, and then using the positioner's inverse kinematics to establish the corresponding (x, y, θ) inputs. The output range of each actuator was divided into eleven increments, corresponding to 1,331 test points.

The errors between the desired position and the measured position (via (3)-(5)) are shown in Fig. 6. Similarly, the rotations of the measurement platforms, corresponding to the misalignment of the interferometer laser beams, against the X position are shown in Fig. 7.

It can be seen from Figs. 6 and 7 that the errors are linearly related to the input positions. The error (or platform rotation) for the parameter p can therefore be expressed as:

$$E_p = a_{x,p}x + a_{y,p}y + a_{\theta,p}\theta \quad (10)$$

Least-squares regression has been utilized to identify the constant parameters for each variable, using the results of the computational study, which are presented in Table 4. The last column provides the RMS error between the measured and the fitted errors. It can be seen that the errors can be predicted with high accuracy using the linear fit.

5.2 Stress Analysis

The equivalent von Mises stress has been predicted at the extreme points of the designed working range. It was observed that the maximum stress occurred at one of the two flexure hinges. As a consequence, the maximum stress was strongly correlated to the θ position. At a 4.12 mrad rotational

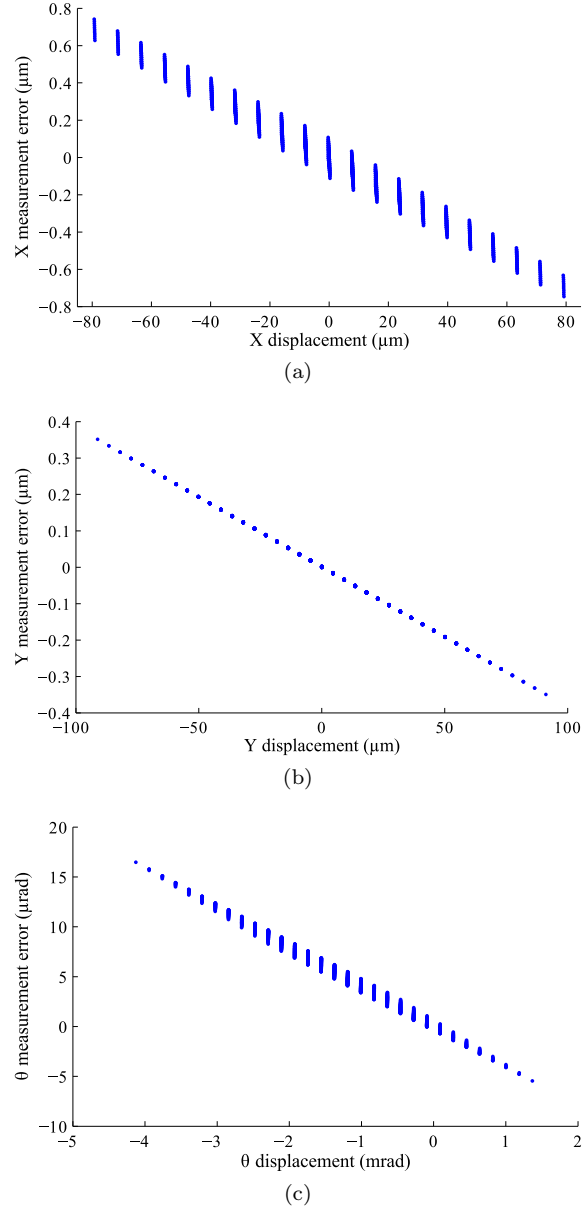


Figure 6: Errors in measurement predicted using computational analysis: (a) X -error, (b) Y -error, (c) θ -error.

displacement, the maximum stress was predicted to be 103.2 MPa, which is about 20% of the yield stress of the material.

5.3 Dynamic Response

A three-dimensional modal analysis was performed to determine the dynamic behavior of the mechanism. The mechanism was meshed with 135,792 elements, again with a refined mesh in proximity to the compliant elements. Fig. 8 shows the first six modes determined from this analysis. It can be seen that the first three modes correspond to motion along the desired measurement axes. Importantly, the

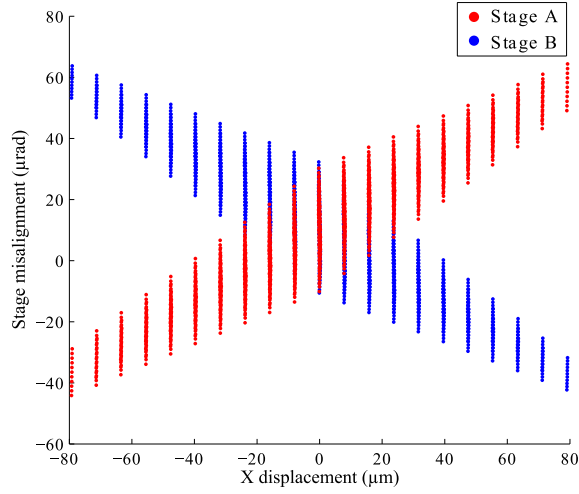


Figure 7: Misalignment of measurement platforms predicted using computational analysis.

Table 4: Regression of error surfaces

	$a_{x,p}$	$a_{y,p}$	$a_{\theta,p}$	RMS error
E_x	-0.00868	-0.00119	1.76×10^{-6}	2.41×10^{-15} m
E_y	-7.86×10^{-6}	-0.00384	-6.03×10^{-7}	1.10×10^{-15} m
E_θ	-0.00781	-0.00578	-0.00399	2.82×10^{-13} rad
α_A	0.588	0.0180	-0.00737	3.21×10^{-13} rad
α_B	-0.603	-0.0394	-0.00778	3.34×10^{-13} rad

higher-order modes have much greater natural frequencies by comparison, reducing the likelihood of their undesirable motions being excited and having an impact on measurement.

6 Experimental Results

Through the computational study, it was found that the measurement errors could be described accurately as linear functions. Hence, experimentation was performed to replicate the computational study of the error variation, and validate this observation in practice. Specifically, the aim of the experiments was to show that the error between the true positioner pose and those predicted with the desired kinematics could be accurately modeled with linear functions.

6.1 Experimental Apparatus

A prototype of the mechanism has been manufactured and mounted on a three DOF positioning stage, as shown in Fig. 9. It has been fabricated using 3D printing techniques, which have been demonstrated to be suitable for the manufacture of compliant mechanisms [38]. The prototype was fabricated using an Objet Eden 260V printer, which prints with a resolution of $42 \mu\text{m}$ in the X - Y plane and $16 \mu\text{m}$ in the Z direction. To accommodate the use of these techniques, flexure elements were thickened allowing more straightforward removal of support material. The use of a different material

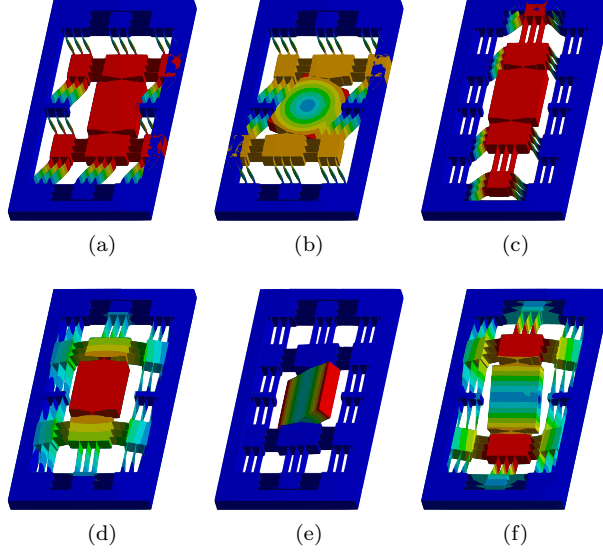


Figure 8: First six natural modes of the mechanism: (a) X -motion (99 Hz), (b) θ -motion (126 Hz), (c) Y -motion (283 Hz), (d)–(f) Out-of-plane motions (1.27 kHz, 1.75 kHz, 2.11 kHz).

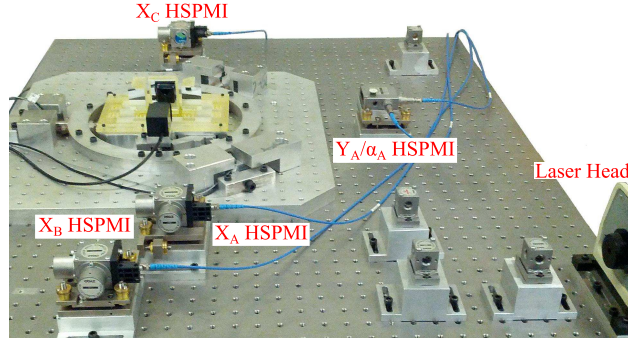
with a modified geometry allowed the ability to calibrate measurement errors to be tested under more uncertain conditions. The material utilized was a UV cured plastic, Polyjet RGD720, with density approximately 1.19 g/cm^3 , elastic modulus 2.5 GPa and 50 MPa tensile strength. T-shaped grooves were added to each platform to permit press-fit mirror mounts (also 3D printed).

The three DOF positioning stage, which has its end effector coupled to the central platform of the passive mechanism, is a flexure-based manipulator based upon the 3-RRR parallel kinematic chain [39]. It is driven by three PEAs, with integrated strain gauge sensors, mounted around the circumference of the base. The mounting of the passive mechanism is such that there is no interference between the two mechanisms other than at the central coupling. Long grooves have been added parallel to the long edge of the mechanism, producing very tall leaf hinges, which are shown in the inset within Fig. 9b. These are intended to reduce out-of-plane moments being transferred in the coupling between the two mechanisms.

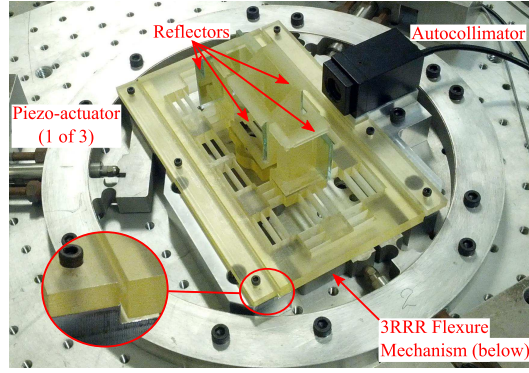
In order to compare the predictions of (3), (4), and (5) with the true position of the stage, a combination of a laser interferometry based measurement and a digital autocollimator was utilized. The laser setup employs five high stability plane mirror interferometer (HSPMI) axes; four linear and one angular. The Y displacement of the central platform could not be measured due to the reflectors on each measurement platform obstructing any interferometer beams in the Y direction. Instead, focus has been placed on the measurement of the X displacements. The arrangement of the interferometer axes is shown in Fig. 9a. A digital autocollimator (Micro-Radian T30D) capable of pitch and yaw measurement is also utilized to measure the central platform yaw.

6.2 Comparative Experimental Cases

Due to the large rotation of the central platform, the X_C axis laser beam was misaligned to such an extent that it ceased to produce viable measurements. As a result, two different experimental cases were considered. The first included positions spanning the full workspace, where X_C measurements were unavailable, whilst the second was restricted to the workspace with zero yaw.



(a)



(b)

Figure 9: Photograph of the experimental apparatus: (a) Full view including laser interferometry based sensing and measurement setup, (b) Close view of flexure mechanisms. The inset shows the elongated leaf hinge for the mechanism's mounting.

In both cases, a trajectory was formed within the actuator space. As with the computational study, for the full workspace each actuator's range divided into ten incremental positions. The trajectory traversed all possible combinations of these positions, providing a dataset of 1000 points. For the 2D (zero yaw) trajectory, points were uniformly spaced in the workspace restricted to the X - Y plane. To construct this trajectory, 145 points were transformed to the required actuator positions using the inverse kinematics. For both trajectories, points were traversed linearly, where the start and end of each movement was smoothed with quadratic sections. The mechanism was halted at each point for the collection of measurements. During this period, the data acquisition commenced after a delay to ensure the decay of any transient movement. For each position measured, 0.45 s was taken for the traversal phase, before the delay of 0.15 s and 0.2 s for data collection. The overall traversal time for each trajectory was approximately 810 s and 125 s for the 3D and 2D trajectories, respectively. About 50 samples were taken at each position, which were averaged to provide the final data point. After averaging, the steady state RMS noise was recorded to be below 2.9 nm in the linear interferometer axes, 0.011 μrad in the angular axis, and 1.1 μrad for the autocollimator.

To minimize the effects of hysteresis on the actuation, and hence increase uniformity in the sampling of positions, feedback control has been employed for the PEA positioning. Proportional-Integral (PI) control with a linear feedforward term was utilized, with feedback provided by the integrated strain gauges.

Fig. 10 shows a comparison of the actual measured X position of the central platform with the position calculated using (3), where measurements were taken over the 2D workspace. For comparison, the

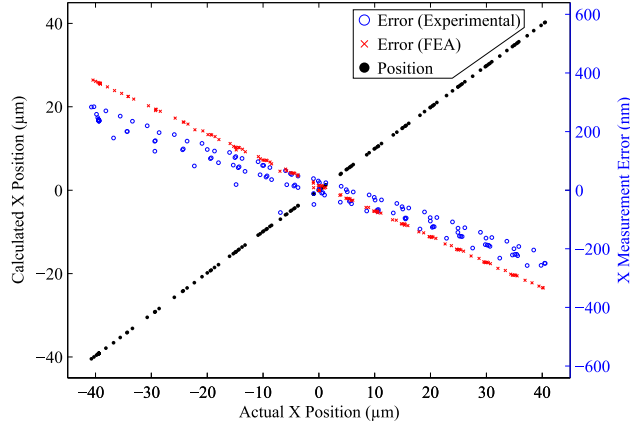


Figure 10: Comparison of the uncalibrated calculated X position of the central platform with that directly measured, where the mechanism has approximately zero yaw.

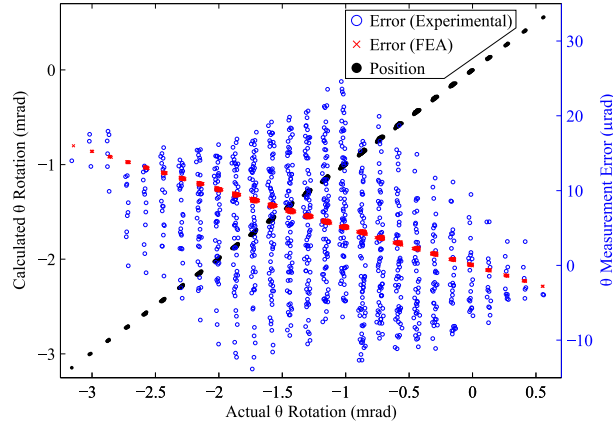


Figure 11: Comparison of the uncalibrated calculated θ position of the central platform with that directly measured.

computational prediction of the error for the prototype is also shown, where the material properties of the photopolymer have been considered within the simulation. Rotational movement in the yaw axis was measured to be below $38.5 \mu\text{rad}$ during this trial.

Similarly, Fig. 11 provides a comparison between the stage yaw and the computation of (5) over the full workspace. The misalignment of the upper platform against the calculated X position is shown in Fig. 12. Throughout the workspace, the misalignment remained beneath $88.8 \mu\text{rad}$.

In both cases it can be seen that the calculated and actual positions agree, where the error is approximately proportionate to the position. The proportionality constants between the actual and calculated positions were 0.9940 for X and 0.9958 for θ . Differences to the computational prediction, particularly the discrepancies in the slopes of the errors, are likely to be due to inaccurate knowledge of the elastic modulus, and manufacturing imperfections.

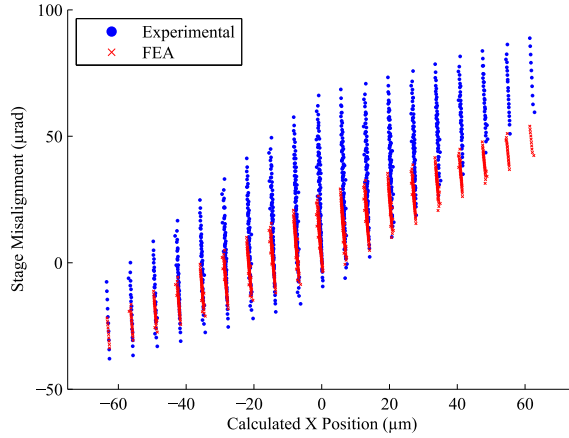


Figure 12: Measured misalignment of the upper measurement platform.

Table 5: Errors and misalignment during calibration

	X_{error}	θ_{error}	α_A
Uncalibrated (max.)	285 nm	25 μrad	88.80 μrad
Calibrated (max.)	79 nm	7 μrad	1.75 μrad
Calibrated (RMS)	20 nm	2.3 μrad	0.56 μrad
Drift during sampling	144 nm	23 μrad	0.41 μrad

7 Discussion

7.1 Calibration

The small RMS residuals in Table 4 show that the measurement errors are a linear function of the actual position of the central platform. This has several implications upon the implementation of such a mechanism for three DOF measurement. Firstly, (10) can be restated in matrix form:

$$\begin{bmatrix} x \\ y \\ \theta \end{bmatrix} = \begin{bmatrix} x_c \\ y_c \\ \theta_c \end{bmatrix} + \begin{bmatrix} a_{xx} & a_{yx} & a_{\theta x} \\ a_{xy} & a_{yy} & a_{\theta y} \\ a_{x\theta} & a_{y\theta} & a_{\theta\theta} \end{bmatrix} \begin{bmatrix} x \\ y \\ \theta \end{bmatrix} \quad (11)$$

This matrix equation can be inverted, hence the predictability of the errors allows the measured and true positions to be related:

$$\begin{bmatrix} x \\ y \\ \theta \end{bmatrix} = \left(I_{3 \times 3} - \begin{bmatrix} a_{xx} & a_{yx} & a_{\theta x} \\ a_{xy} & a_{yy} & a_{\theta y} \\ a_{x\theta} & a_{y\theta} & a_{\theta\theta} \end{bmatrix} \right)^{-1} \begin{bmatrix} x_c \\ y_c \\ \theta_c \end{bmatrix}. \quad (12)$$

A summary of the maximum errors in the output positions with and without this calibration is provided in Table 5. In particular, the errors seen in Figs. 10, 11 and 12 are all significantly reduced by the calibration.

As the errors can be modelled accurately with linear functions, it may be possible to perform calibration within a reduced range. This would allow existing measurement techniques, which may have

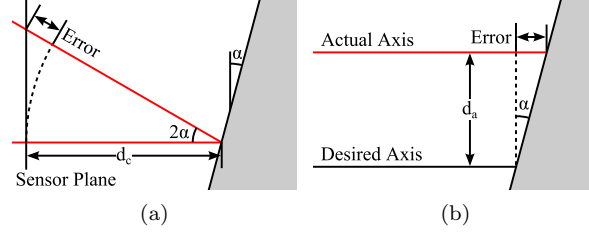


Figure 13: Geometric errors in laser interferometry based measurement: (a) Cosine error, (b) Abbe error.

insufficient range for the full workspace, to be used as reference sensors. The linearity of the error variation would ensure that the small-scale calibration could be extended to the passive mechanism's working range. Similarly, with more accurate knowledge of the elastic modulus of the material, the qualitative agreement between the experimental study and finite element modelling could facilitate partial calibration using the computational predictions.

The platform misalignment was seen to be mostly dependent on the X motion. As seen in Fig. 7, at the boundary of the workspace, the misalignment was predicted to be about $60 \mu\text{rad}$. This can potentially give rise to geometric errors within the laser interferometry based sensing and measurement system. These are shown schematically in Fig. 13. The magnitudes of these cosine and Abbe errors can be estimated via the following equations:

$$\Delta x_{\text{Abbe}} = d_a \tan \alpha \approx d_a \alpha \quad (13)$$

$$\Delta x_{\text{cosine}} = d_c (\sec 2\alpha - 1) \approx 2d_c \alpha^2 \quad (14)$$

As the largest d_c within the experimental setup was 418 mm, the greatest cosine error was predicted to be 6.6 nm. The Abbe errors were much greater, scaling as a linear function of α . It is therefore very important to minimize d_a , the distance separating the measurement axis from the coordinate axis. In this experimental setup, the largest separation was 16 mm, hence the maximum Abbe error was $1.4 \mu\text{m}$. However, as it is possible to predict α using (10), these Abbe errors can be compensated. Using the calculated positions (through (3), (6) and (5)), a least-squares linear fit of α_A was found. The error in this linear fit was below $1.75 \mu\text{rad}$. Hence, after compensation it can be expected that a residual uncertainty of 28 nm remains, which can be improved through reduction of the separation d_a .

7.2 Limitations of Experiments

Although similar trends can be observed between the computational and experimental studies, the prototype did not perform as well as predicted. This is especially evident in the θ error in Fig. 11. It should be noted that the θ error has a greater dependence on X and Y compared with the computational predictions, which are not shown in this figure. Despite this, the correction given by (12) was still effective; the maximum error after calibration was $7 \mu\text{rad}$. Furthermore, the calculated θ error (shown in Fig. 11) has a significant component resulting from the uncertainty in both the autocollimator and the interferometer measurements.

As shown in Table 5, the errors after correction are still relatively large compared with the steady state noise level. As only the PEA inputs to the 3-RRR mechanism were controlled, instead of the output positions, measurements were observed to drift during acquisition. The mean drift in each X , θ and α_A datapoint is shown in Table 5. As the mean of the 50 samples was used for each point, the uncertainty in the true position would be lower than these values, nonetheless the drift is the main

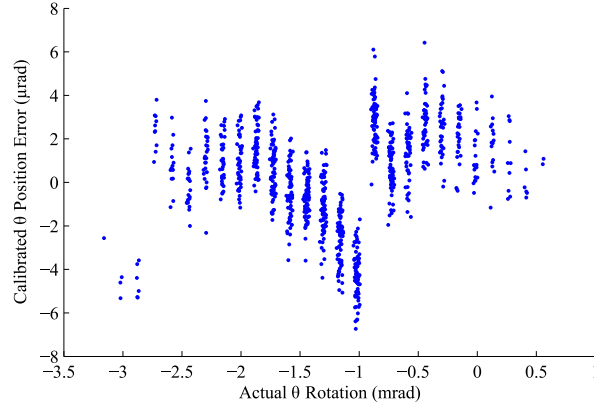


Figure 14: Residual error after calibration of θ position of the central platform.

contributor to the residual error for the results presented. The drift could be reduced with a slower traversal, however this would have made the duration of these experiments prohibitively long. Hence, to within the capabilities of the experimental apparatus, it has been observed that measurement errors can be reduced through calibration.

Performance may be improved if the mechanism were fabricated from a metallic or alloy-based material, as was assumed in the initial computational analysis. In particular, the fabrication of the prototype from plastic material may have introduced hysteresis into the mechanism's behaviour. Fig. 14 shows the post-calibration measurement error, from which it is clear that an underlying non-linear variation is present.

7.3 Influence on Dynamic Response

The coupling of the passive mechanism to the positioning stage may have an unwanted influence on the dynamic response. Moreover, the first natural frequency may be lowered which would reduce the bandwidth of measurable motions. Approximating the first mode of both systems as simple second order oscillators, the coupling of the passive mechanism can be considered as adding the mass M_m to the positioning stage's mass M_p , whilst also adding a spring k_m in parallel to the existing flexures, which have stiffness k_p . This is a reasonable assumption when the first mode of the positioner is an oscillation along the X axis. In the case of the 3-RRR positioner, the first three modes align with those of the passive mechanism. The characteristic equation of the oscillator, with some damping b , can then be expressed as:

$$p(s) = (M_m + M_p)s^2 + bs + (k_m + k_p) \quad (15)$$

Hence the resonant frequency ω_T can be predicted using (16):

$$\begin{aligned} \omega_T &= \sqrt{\frac{k_m + k_p}{M_m + M_p}} \\ &= \omega_m \sqrt{\frac{M_p \rho^2 + M_m}{M_p + M_m}} \end{aligned} \quad (16)$$

where ρ is the ratio between ω_p and ω_m . So long as the passive mechanism has a higher first natural frequency than the positioner, it can be seen that the combined natural frequency will not be lowered due to the coupling.

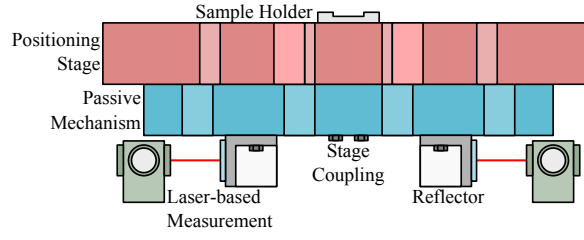


Figure 15: Schematic for utilizing passive mechanism within a sample positioning system.

7.4 Considerations for Potential Applications

It should be noted that the use of the 3-RRR stage was purely as an illustrative planar three DOF positioner. Accordingly, as the maximum stress predicted within the 3-RRR positioner’s workspace was lower than the yield strength, the same mechanism could potentially be coupled to other positioners with a much larger working range. Similar performance would be expected within the linear elastic range of the material. It is anticipated that the proposed mechanism topology could have general application for all high-precision planar positioners.

The goal of the optimization procedure was to reduce the magnitude of each entry a_{ij} as much as possible. However, so long as these entries can be accurately determined through calibration, the optimization procedure can be reformulated. For example, alternative optimization strategies could utilize a cost function emphasizing the minimization of stress or the measurement platform misalignment. In this study, the size of the mechanism was chosen to accommodate the 3-RRR positioner (about $195 \text{ mm} \times 133 \text{ mm} \times 14 \text{ mm}$). Due to the ability to perform calibration, it is anticipated that similar performance would be exhibited for scaled down variants employed for more compact stages.

The computational stress analysis showed that the maximum stresses at a maximum rotation of 4.12 mrad from the zero position were about 20% of the yield stress of the material. This led to limitations on the working range of the mechanism. From the optimization procedure, it was found that for greater rotational precision of the hinges, the thickness needed to be reduced, whilst the hinge geometry approached that of a V-hinge. This would in turn increase the maximum stresses within the hinge. As a consequence of the discussion above, where the errors can be easily compensated, it can be seen that the hinges can be thickened, which will allow the working range to be increased.

It is foreseen that the passive mechanism could be incorporated into the design of a positioning system. For potential uses such as within scanning microscopes, the passive mechanism could be mounted on the reverse side of the sample stage, as shown in Fig. 15. Similarly, with rapid prototyping techniques gaining prominence, it could be possible to manufacture the measurement component and the positioning components of the system as a monolithic mechanism. In particular, this would allow the dynamics of the coupled system to be predicted computationally during the design phase.

8 Conclusions

This paper presented the design of a passive compliant mechanism which transforms planar three DOF motions into linear motions measurable by laser interferometer based sensing techniques. A computational optimization methodology was introduced to achieve the desired kinematic relationships. A computational study of the final design demonstrated that errors in measurement, in addition to the misalignment of the measurement platforms, could be modeled accurately, and hence error compensation is feasible. Furthermore, the ability to compensate for such errors gives the freedom to modify the design, even if the kinematic relations are not exactly satisfied. Whilst limited by undesirable material

behavior, experimental results demonstrated that the measurement of three DOF motions could be achieved utilizing this design methodology, with errors minimized through calibration.

Acknowledgment

The authors would like to thank Mr. Soon Hock Ng from the Melbourne Center for Nanofabrication (MCN) for his assistance in the fabrication of the prototype.

References

- [1] B. J. Kenton and K. K. Leang, "Design and control of a three-axis serial-kinematic high-bandwidth nanopositioner," *IEEE/ASME Trans. Mechatronics*, vol. 17, no. 2, pp. 356–369, 2012.
- [2] W. Chen, X. Shi, W. Chen, and J. Zhang, "A two degree of freedom micro-gripper with grasping and rotating functions for optical fibers assembling," *Review of Scientific Instruments*, vol. 84, no. 11, p. 115111, 2013.
- [3] Y. Tian, D. Zhang, and B. Shirinzadeh, "Dynamic modelling of a flexure-based mechanism for ultra-precision grinding operation," *Precision Engineering*, vol. 35, no. 4, pp. 554–565, 2011.
- [4] J. Guo, H. Suzuki, S.-y. Morita, Y. Yamagata, and T. Higuchi, "A real-time polishing force control system for ultraprecision finishing of micro-optics," *Precision Engineering*, vol. 37, no. 4, pp. 787–792, 2013.
- [5] M. N. M. Zubir, B. Shirinzadeh, and Y. Tian, "A new design of piezoelectric driven compliant-based microgripper for micromanipulation," *Mechanism and Machine Theory*, vol. 44, no. 12, pp. 2248–2264, 2009.
- [6] Z. Wen, Z. Dong, P. Liu, and H. Ding, "Design of a fine alignment system featuring active orientation adjustment for nano imprint lithography," *Review of Scientific Instruments*, vol. 85, no. 3, p. 035106, 2014.
- [7] Y. Tian, B. Shirinzadeh, D. Zhang, X. Liu, and D. Chetwynd, "Design and forward kinematics of the compliant micro-manipulator with lever mechanisms," *Precision Engineering*, vol. 33, no. 4, pp. 466–475, 2009.
- [8] Y. Li and Q. Xu, "A totally decoupled piezo-driven XYZ flexure parallel micropositioning stage for micro/nanomanipulation," *IEEE Trans. Autom. Sci. Eng.*, vol. 8, no. 2, pp. 265–279, 2011.
- [9] C.-X. Li, G.-Y. Gu, M.-J. Yang, and L.-M. Zhu, "Design, analysis and testing of a parallel-kinematic high-bandwidth XY nanopositioning stage," *Review of Scientific Instruments*, vol. 84, no. 12, p. 125111, 2013.
- [10] Y. Qin, B. Shirinzadeh, Y. Tian, D. Zhang, and U. Bhagat, "Design and computational optimization of a decoupled 2-DOF monolithic mechanism," *IEEE/ASME Trans. Mechatronics*, vol. 19, no. 3, pp. 872–881, 2014.
- [11] Y. Tian, B. Shirinzadeh, D. Zhang, and Y. Zhong, "Three flexure hinges for compliant mechanism designs based on dimensionless graph analysis," *Precision Engineering*, vol. 34, no. 1, pp. 92–100, 2010.
- [12] R. Wang, X. Zhou, and Z. Zhu, "Development of a novel sort of exponent-sine-shaped flexure hinges," *Review of Scientific Instruments*, vol. 84, no. 9, p. 095008, 2013.

- [13] H. C. Liaw and B. Shirinzadeh, "Robust adaptive constrained motion tracking control of piezo-actuated flexure-based mechanisms for micro/nano manipulation," *IEEE Trans. Ind. Electron.*, vol. 58, no. 4, pp. 1406–1415, 2011.
- [14] G.-y. Gu, L.-m. Zhu, C.-y. Su, H. Ding, and S. Fatikow, "Proxy-based sliding-mode tracking control of piezoelectric-actuated nanopositioning stages," *IEEE/ASME Trans. Mechatronics*, vol. 20, no. 4, pp. 1956–1965, 2015.
- [15] U. Bhagat, B. Shirinzadeh, L. Clark, Y. Qin, Y. Tian, and D. Zhang, "Experimental investigation of robust motion tracking control for a 2-DOF flexure-based mechanism," *IEEE/ASME Trans. Mechatronics*, vol. 19, no. 6, pp. 1737–1745, 2014.
- [16] Y. Cao, L. Cheng, X. B. Chen, and J. Y. Peng, "An Inversion-Based Model Predictive Control With an Integral-of-Error State Variable for Piezoelectric Actuators," *IEEE/ASME Trans. Mechatronics*, vol. 18, no. 3, pp. 895–904, 2013.
- [17] H. C. Liaw, B. Shirinzadeh, and J. Smith, "Robust neural network motion tracking control of piezoelectric actuation systems for micro/nanomanipulation," *IEEE Trans. Neural Netw.*, vol. 20, no. 2, pp. 356–367, 2009.
- [18] L.-S. Chen, J.-Y. Yen, J. J. Chen, F.-C. Kuo, M.-S. Chen, Y.-Y. Chen, and B.-I. Chung, "Precision tracking of a piezo-driven stage by charge feedback control," *Precision Engineering*, vol. 37, no. 4, pp. 793–804, 2013.
- [19] Y. Qin, Y. Tian, D. Zhang, B. Shirinzadeh, and S. Fatikow, "A novel direct inverse modeling approach for hysteresis compensation of piezoelectric actuator in feedforward applications," *IEEE/ASME Trans. Mechatronics*, vol. 18, no. 3, pp. 981–989, 2013.
- [20] M. A. Janaideh and P. Krejčí, "Inverse rate-dependent Prandtl Ishlinskii model for feedforward compensation of hysteresis in a piezomicropositioning actuator," *IEEE/ASME Trans. Mechatronics*, vol. 18, no. 5, pp. 1498–1507, 2013.
- [21] U. Bhagat, B. Shirinzadeh, Y. Tian, and D. Zhang, "Experimental analysis of laser interferometry-based robust motion tracking control of a flexure-based mechanism," *IEEE Trans. Autom. Sci. Eng.*, vol. 10, no. 2, pp. 267–275, 2013.
- [22] Z. Du, Y. Su, W. Yang, and W. Dong, "Note: a piezo tip/tilt platform: structure, kinematics, and experiments," *Review of Scientific Instruments*, vol. 85, no. 4, p. 046102, 2014.
- [23] H.-J. Lee, H.-C. Kim, H.-Y. Kim, and D.-G. Gweon, "Optimal design and experiment of a three-axis out-of-plane nano positioning stage using a new compact bridge-type displacement amplifier," *Review of Scientific Instruments*, vol. 84, no. 11, p. 115103, 2013.
- [24] D. Kang, K. Kim, Y.-M. Choi, D. Gweon, S. Lee, and M. Lee, "Design and control of flexure based XYθz stage," *Journal of Mechanical Science and Technology*, vol. 19, no. 11, pp. 2157–2164, 2005.
- [25] H.-Y. Kim, D.-H. Ahn, and D.-G. Gweon, "Development of a novel 3-degrees of freedom flexure based positioning system," *Review of Scientific Instruments*, vol. 83, no. 5, p. 055114, 2012.
- [26] Y. K. Yong and T.-F. Lu, "Kinetostatic modeling of 3-RRR compliant micro-motion stages with flexure hinges," *Mechanism and Machine Theory*, vol. 44, no. 6, pp. 1156–1175, 2009.
- [27] U. Bhagat, B. Shirinzadeh, L. Clark, P. Chea, Y. Qin, Y. Tian, and D. Zhang, "Design and analysis of a novel flexure-based 3-DOF mechanism," *Mechanism and Machine Theory*, vol. 74, pp. 173–187, 2014.
- [28] J. Yuan and X. Long, "CCD-area-based autocollimator for precision small-angle measurement," *Review of Scientific Instruments*, vol. 74, no. 3, p. 1362, 2003.

- [29] F. Cheng and K.-C. Fan, “High-resolution angle measurement based on Michelson interferometry,” *Physics Procedia*, vol. 19, pp. 3–8, 2011.
- [30] Z. Ge and M. Takeda, “High-resolution two-dimensional angle measurement technique based on fringe analysis,” *Applied optics*, vol. 42, no. 34, pp. 6859–68, 2003.
- [31] M. Pisani and M. Astrua, “Angle amplification for nanoradian measurements,” *Applied optics*, vol. 45, no. 8, pp. 1725–9, 2006.
- [32] J.-W. Kim, C.-S. Kang, J.-A. Kim, T. Eom, M. Cho, and H. J. Kong, “A compact system for simultaneous measurement of linear and angular displacements of nano-stages,” *Optics express*, vol. 15, no. 24, pp. 15 759–66, 2007.
- [33] J.-h. Zhang and C.-H. Menq, “A linear/angular interferometer capable of measuring large angular motion,” *Measurement Science and Technology*, vol. 10, no. 12, pp. 1247–1253, 1999.
- [34] H.-C. Yeh, W.-T. Ni, and S.-S. Pan, “Real-time motion control with subnanometer heterodyne interferometry,” *International Journal of Modern Physics D*, vol. 11, no. 07, pp. 1087–1099, 2002.
- [35] J. Hrabina, J. Lazar, P. Klapetek, and O. Číp, “Multidimensional interferometric tool for the local probe microscopy nanometrology,” *Measurement Science and Technology*, vol. 22, no. 9, p. 094030, 2011.
- [36] J. Lazar, P. Klapetek, O. Číp, M. Čížek, and M. Šerý, “Local probe microscopy with interferometric monitoring of the stage nanopositioning,” *Measurement Science and Technology*, vol. 20, no. 8, p. 084007, 2009.
- [37] L. Clark, B. Shirinzadeh, Y. Tian, and D. Oetomo, “Laser-based sensing, measurement, and misalignment control of coupled linear and angular motion for ultrahigh precision movement,” *IEEE/ASME Trans. Mechatronics*, vol. 20, no. 1, pp. 84–92, 2015.
- [38] U.-X. Tan, W. T. Latt, C. Y. Shee, and W. T. Ang, “A Low-Cost Flexure-Based Handheld Mechanism for Micromanipulation,” *IEEE/ASME Trans. Mechatronics*, vol. 16, no. 4, pp. 773–778, 2011.
- [39] Y. Tian, B. Shirinzadeh, and D. Zhang, “Design and dynamics of a 3-DOF flexure-based parallel mechanism for micro/nano manipulation,” *Microelectronic Engineering*, vol. 87, no. 2, pp. 230–241, 2010.